Gate-Tunable Near-Field Heat Transfer

Georgia T. Papadakis, Bo Zhao, Siddharth Buddhiraju, and Shanhui Fan*

Department of Electrical Engineering, Ginzton Laboratory, Stanford University, Stanford, California 94305, United States

ABSTRACT: Active control over the flow of heat in the near-field holds promise for nanoscale thermal management, with applications in refrigeration, thermophotovoltaics, and thermal circuitry. Analogously to its electronic counterpart, the metal–oxide–semiconductor (MOS) capacitor, we propose a thermal switching mechanism based on accumulation and depletion of charge carriers in an ultrathin plasmonic film, via application of external bias. In our proposed configuration, the plasmonic film is placed on top of a polaritonic dielectric material that provides a surface phonon polariton (SPhP) thermal channel, while also ensuring electrical insulation for application of large electric fields. The variation of carrier density in the plasmonic film enables the control of the surface plasmon polariton (SPP) thermal channel. We show that the interaction of the SPP with the SPhP significantly enhances the net heat transfer. We study SiC as the oxide and explore three classes of gate-tunable plasmonic materials, transparent conductive oxides, doped semiconductors, and graphene, and theoretically predict contrast ratios as high as 225%.

KEYWORDS: *thermal radiation, field effect, ITO, graphene*
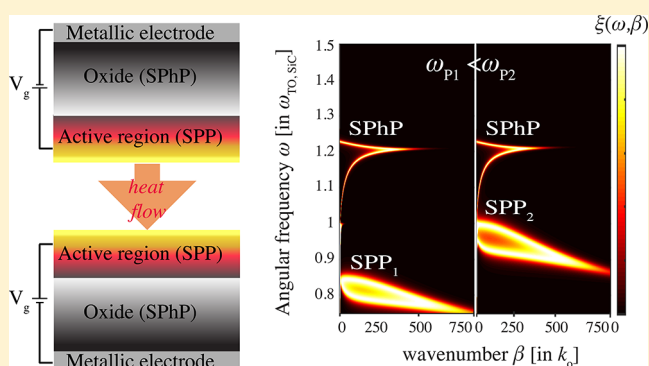
Controlling the flow of an electric current is the cornerstone of modern optoelectronics and is ubiquitous in a wide range of applications from data processing and telecommunications to energy conversion. Analogously, actively tailoring the flow of heat is of fundamental importance in thermal management and recycling. A significant volume of work has focused on radiative heat transfer, where active modulation relies on controlling photon heat flux.[1−9] In contrast to the far-field, where the Stefan–Boltzmann law of thermal radiation imposes an upper bound to the amount of photon heat flux exchanged between two objects, in the near-field, evanescent wave tunneling can yield significantly larger heat exchange.[1,10−13] Thus, it is of importance to control radiative heat flux in the near-field, with potential applications in thermal circuitry,[14,15] thermal energy harvesting and recycling,[2,16−18] refrigeration,[19] and nanoscale thermal imaging.[20,21]

Since the 1950s, the metal−oxide−semiconductor (MOS) device has been at the heart of solid-state electronic operations.[22,23] In a MOS device, such as the metal-oxide-semiconductor field effect transistor (MOSFET), voltage gating of a semiconductor against a metallic electrode separated by an oxide layer results in accumulation and depletion of charge carriers. This in turn leads to changes in the electrical conductivity of the active region and hence the operation of an electrical switch.

Analogously, to create a switch for photon-based heat flux, one will need materials for which their photonic properties can be tuned. Previous considerations in radiative thermal switching have focused on phase change materials, such as vanadium oxide, or phase change ferroelectric materials such as perovskites, as crystallographic phase changes are typically accom-

panied by changes in optical properties.[14,15,24−30] However, despite the pronounced crystallographic changes occurring near a phase transition, changes in optical properties, e.g., dielectric permittivity, are typically moderate, leading to relatively modest contrast ratios, for example a 17% tunability range in photon heat flux reported in ref 30. Another strategy is the application of an external magnetic field in magneto-optical material systems, in which case control of either the amplitude or the direction of the magnetic field can analogously alter their optical properties and, in turn, their radiative heat conductance.[31−35] Alternative mechanisms for tuning near-field heat transfer include photo-excitation[36] and nonlinear processes,[37] which, however, require large optical power densities beyond the kW/cm² range. Graphene's carrier density-tunable optical response has also been proposed as a heat flux modulating mechanism;[38−43] however a realistic configuration for practical carrier injection and corresponding electrostatic considerations have not been discussed.

In this paper, we show that the concept of an MOS capacitor, as is widely used in electronic switching, can be alternatively used as a thermal MOS switch that achieves significant switching of photon heat flux by controlling a gate bias. An advantage of our proposed scheme compared to previous considerations for tuning photon heat flux lies in its simplicity, since field effect gating of a MOS capacitor constitutes a widespread and robust mechanism for tuning the properties of thin films and planar optoelectronic modules.[44] In terms of contrast ratios, our thermal MOS switch significantly outperforms previous

proposals, with switching (ON/OFF) ratios reaching 225% in some of our designs. Analogously to the electronic MOS, the underlying mechanism lies in controlling the charge carrier density in an ultrathin heavily doped semiconductor layer gated against a metallic electrode. Changes in carrier density in such an ultrathin layer affect the plasmon supported by the layer, which is designed to be spatially confined in the active region of the thermal MOS (red region in Figure 1), therefore yielding large
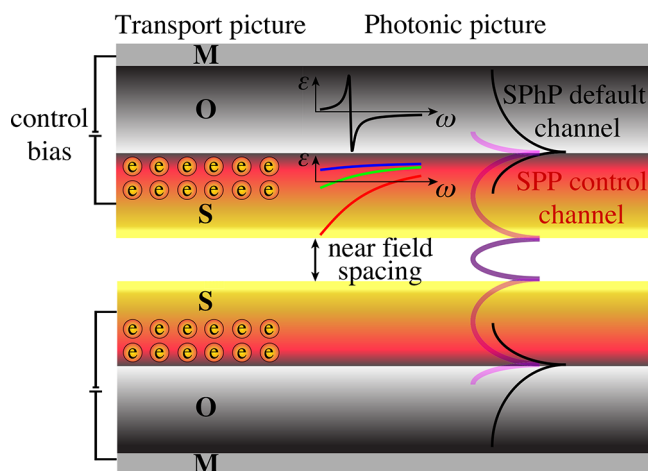

Figure 1. Thermal metal (M)−oxide (O)−semiconductor (S) switch. Application of an external voltage across the oxide can alter the charge carrier density in the vicinity of the semiconductor/oxide interface. Schematic depicts either an n-doped semiconductor in accumulation mode or a p-doped semiconductor in depletion mode. Most oxides exhibit optical phonons in their crystal structure, which yield Lorentz-type polaritonic permittivity resonances (black ϵ curve), and corresponding surface phonon polariton (SPhP) evanescent modes. Free charge carriers in the semiconductor/oxide interface yield a metallic response that depends on the carrier density. Green permittivity curve corresponds to the absence of control bias, whereas blue and red curves correspond to operation in depletion and accumulation, respectively. A tunable surface plasmon polariton (SPP) channel in the active region controls the thermal properties of the module.

sensitivity to the control bias. This is to be contrasted with previous reports on gate-tunable response in the far-field,[45,46] where emission and absorption are moderately modulated via changes in optical properties, since radiative modes that manifest the far-field response of a photonic material are, by nature, not necessarily spatially confined to the miniscule size of the active region. By placing two such MOS capacitors in close proximity, as shown in Figure 1, the heat transfer between the two capacitors is then actively controlled via a gate bias. In addition to significant contrast ratios, our proposed scheme can lead to CMOS-compatible near-field thermal switching modules, with switching speed that coincides with that of an electronic switch at the GHz level.[47,48] Additionally, operation of the proposed thermal MOS switch requires very low electrostatic power densities on the order of tens of W/cm² for typical MOS device areas that can reach hundreds of μm².[49,50]

Although we refer to the proposed scheme as a thermal "MOS" switch, we note that the "semiconductor" may be any plasmonic material with tunable carrier density. We explore three classes of gate-tunable materials: transparent conductive oxides (TCOs) and nitrides, doped semiconductors, and

monolayer graphene, which support surface plasmon polaritons (SPPs) below their plasma frequency. The "oxide" layer may be any insulating material and may also support a phonon−polaritonic dielectric response. The oxide layer thus may also support a surface phonon polariton (SPhP), which plays a significant role in the near-field heat transfer as well. In this work, we use SiC as the "oxide" layer, and moreover, we also consider near-field heat transfer between two SiC regions as the benchmark with which we compare our thermal switch. The reason for the selection of SiC is twofold: (i) SiC exhibits a high-quality factor resonance[51] that aligns with the peak of blackbody radiation at moderate temperatures, and its SPhP has been widely exploited in the study of near-field heat transfer.[1,3,10−13,52−56] (ii) Apart from its optimal thermal response, SiC is also a good electrical insulator with a breakdown voltage of $E_{br} = 3$ MV/cm (for 4H-SiC, while $E_{br} = 3.2$ MV/cm for 6H-SiC along its optical axis);[57−60] hence it can sustain large electrostatic biases in serving as the "oxide" in the thermal MOS configuration of Figure 1. Aside from SiC, our results can be generalized to other choices of oxides such as silicon dioxide (SiO₂)[12,61] or hexagonal boron nitride (hBN).[40,42]

FORMULATION

To treat the heat transfer in the geometry shown in Figure 1, we employ the standard fluctuational electrodynamics approach. The total heat flux per area exchanged between two bodies at temperatures $T_1 > T_2$, separated by a vacuum gap of thickness d, is given by[1,2,10,11]

$$Q = \frac{1}{4\pi^2} \int_0^\infty d\omega [\Theta(\omega, T_1) - \Theta(\omega, T_2)] S(\omega) \tag{1}$$

where $\Theta(\omega,T) = \hbar\omega/[\exp(\hbar\omega/k_B T) - 1]$ is the mean energy of a harmonic oscillator at frequency ω and temperature T, and $S(\omega)$ is the spectral transfer function. Through the paper, unless otherwise noted, we set $T_1 = 600$ K and $T_2 = 300$ K. For planar configurations,

$$S(\omega) = \int_0^\infty d\beta \, \xi(\omega, \beta) \beta \tag{2}$$

where β is the in-plane wavenumber. The parameter $\xi(\omega, \beta)$ is the photon transmission probability averaged over transverse electric (s) and transverse magnetic (p) polarizations. For separation distances d smaller than the thermal wavelength $\lambda_T = b/T$, where $b = 2989$ μm·K, the evanescent wave's contribution dominates, and

$$\xi(\beta > k_o, \omega) = \frac{4\text{Im}(r_1) \, \text{Im}(r_2) e^{-2|k_{z0}|d}}{|1 - r_1 r_2 e^{-2ik_{z0}d}|^2} \tag{3}$$

In eq 3, $k_0 = \omega/c$ is the free space wavenumber and k_{z0} is the out-of-plane wavenumber in vacuum. The parameters $r_{1,2}$ are the Fresnel reflection coefficients for incidence from the gap (vacuum) to bodies 1 and 2. Bodies 1 and 2 could be either semi-infinite or composed of a multilayer configuration, as in Figure 1. In either case, $r_{1,2}$ can be generally computed with a transfer matrix formalism for layered media.[62,63]

CONCEPT

In this section, we demonstrate that the total heat flux Q exchanged between a pair of semi-infinite plasmonic materials separated by a vacuum gap in the near-field, as shown in the inset of Figure 2a, depends on the plasma frequency, and therefore

depends on the carrier density. This result enables the use of carrier injection to tune near-field heat transfer.

We model the plasmonic dielectric function with the Drude model:

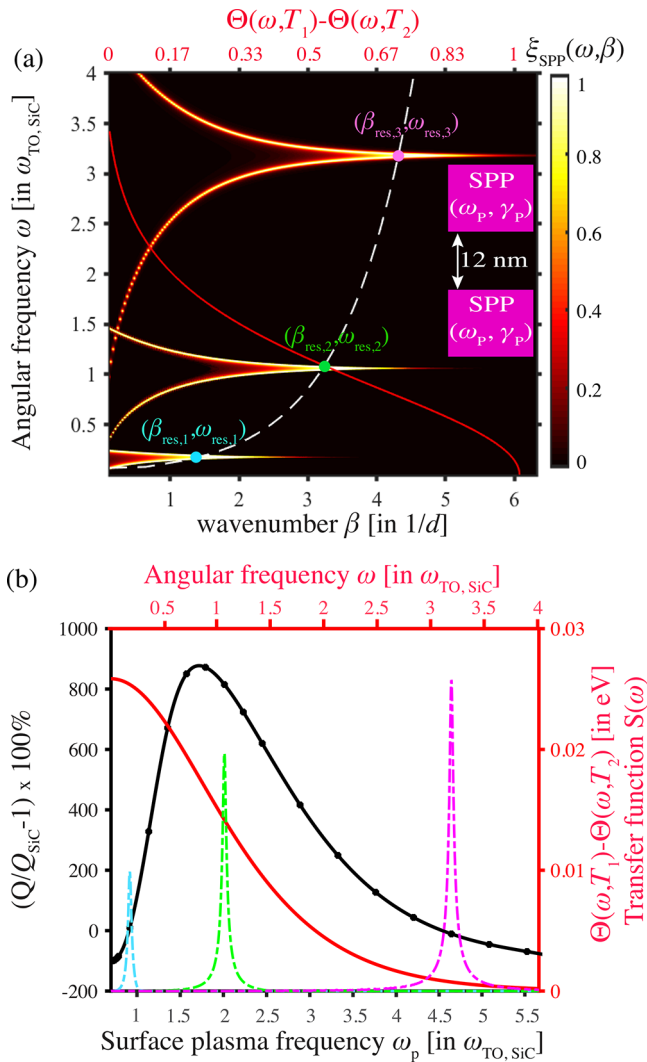$$\epsilon(\omega) = \epsilon_\infty - \frac{\omega_p^2}{\omega^2 + i\omega\gamma_p} \tag{4}$$

Figure 2. Near-field heat transfer between two bulk plasmonic regions as described by the Drude model. (a) Photon transmission probability ξ_{SPP} for a pair of semi-infinite Drude metals separated by $d = 12$ nm, with $\omega_{P1} = 0.25\omega_{TO,SiC}$ (lower curve), $\omega_{P2} = 1.5\omega_{TO,SiC}$ (middle curve), and $\omega_{P3} = 4.5\omega_{TO,SiC}$ (upper curve), for $\gamma_p = 5\gamma_{SiC}$. Red curve (upper horizontal axis) corresponds to the energy exchange per photon $\Theta(\omega,T_1) - \Theta(\omega,T_2)$, for $T_1 = 600$ K and $T_2 = 300$ K, normalized to its value at $\omega = 0$. White dashed line corresponds to eq 7, the wavenumber β_{res} that maximizes near-field heat transfer, as a function of ω_p (the considered range of ω_p is the same as that of ω). Coordinates $(\beta_{res,i}, \omega_{res,i})$ for $i = 1, 2,$ and 3 correspond to the wavenumber and frequency that maximize ξ_{SPP} (eqs 6, 7), for $\omega_{P1}, \omega_{P2},$ and ω_{P3}. (b) Black curve (left vertical axis and corresponding lower horizontal axis): total heat flux (relative to SiC) for increasing ω_p. Red curve (right vertical axis and corresponding upper horizontal axis): $\Theta(\omega,T_1) - \Theta(\omega,T_2)$ in eV. Dashed curves (right vertical axis and corresponding upper horizontal axis): $S(\omega)$ (eq 2), calculated for ω_{P1} (cyan), ω_{P2} (green), and ω_{P3} (magenta). The peak value for the magenta curve is 1.03×10^{16} m^{-2}.

where ω_p is the plasma frequency, γ_p is the momentum-relaxation rate of charge carriers, and ϵ_∞ is the high-frequency dielectric constant. The plasma frequency is given by $\omega_p = \sqrt{Ne^2/\epsilon_o m^*}$, where e is the electron charge, ϵ_o is the free space dielectric constant, m^* is the effective mass of charge carriers, and N is the charge carrier density. Below ω_p, the plasmonic interfaces support p-polarized SPPs, while the contribution from s-polarization may be ignored as there is no s-polarized surface wave in this system.[3,10,64,65] Near the SPP resonance, where the in-plane wavenumber β is large, the Fresnel coefficient becomes $r_{1,2} \approx \frac{\epsilon(\omega)-1}{\epsilon(\omega)+1}$, and the photon transmission probability of eq 3 may be approximated by[64]

$$\xi_{SPP}(\omega) = \frac{16\omega_p^4\gamma_p^2\omega^2}{\Pi(\omega, x)}$$

where

$$\Pi(\omega, x) = 16[(\omega_p^2/2 - \omega^2)^2 + \gamma_p^2\omega^2]^2 e^{2x} -$$
$$8[(\omega_p^2/2 - \omega^2)^2 - \gamma_p^2\omega^2]\omega_p^4 + \omega_p^8 e^{-2x}$$

where we have set $\epsilon_\infty = 1$ and $x = \sqrt{\beta^2 - k_o^2}\,d$. When d is smaller than the thermal wavelength, near-field heat transfer is dominated by contributions from evanescent waves with $\beta \gg k_0$; hence $x \approx \beta d$. The photon transmission probability ξ_{SPP} is upper bounded by unity. By setting ξ_{SPP} to unity, with some algebraic manipulation (see ref 64 for details), we obtain the corresponding wavenumber

$$\beta_{SPP}(\omega) = \frac{1}{2d}\ln\left[\frac{\omega_p^4/4}{(\omega_p^2/2 - \omega^2)^2 + \gamma_p^2\omega^2}\right] \tag{5}$$

In the integrand of eq 2, which determines the spectral transfer function, due to the factor β, the maximum wavenumber where the photon transmission probability remains at unity strongly influences the total magnitude of heat transfer. To determine such a maximum wavenumber we set $\partial\beta_{SPP}/\partial\omega = 0$ to obtain

$$\omega_{res} = \sqrt{\frac{\omega_p^2 - \gamma_p^2}{2}} \tag{6}$$

and, correspondingly, from eq 5,

$$\beta_{SPP}(\omega_{res}) \triangleq \beta_{res} = \frac{1}{d}\ln\left[\left(\frac{\omega_p}{\gamma_p}\right)\frac{1}{2 - (\gamma_p/\omega_p)^2}\right] \tag{7}$$

Here, we refer to the frequency and wavenumber thus obtained (eqs 6, 7) as the resonant frequency and wavenumber, since, as we will see below, the spectral heat flux strongly peaks at such frequencies.

Equation 7 demonstrates that, for ω_p considerably larger than γ_p, the dependence of β_{res} on ω_p is logarithmic. This trend is shown in Figure 2a with the photon transmission probabilities for a pair of semi-infinite plasmonic materials separated by a 12 nm vacuum gap. As mentioned in the introduction, we use SiC parameters as points of reference henceforth. Namely, we normalize the angular frequency, ω, to $\omega_{TO,SiC} = 1.49 \times 10^{14}$ rad/s, the transverse optical phonon frequency of SiC,[52−54] and the total heat flux, Q, to the equivalent configuration separating two
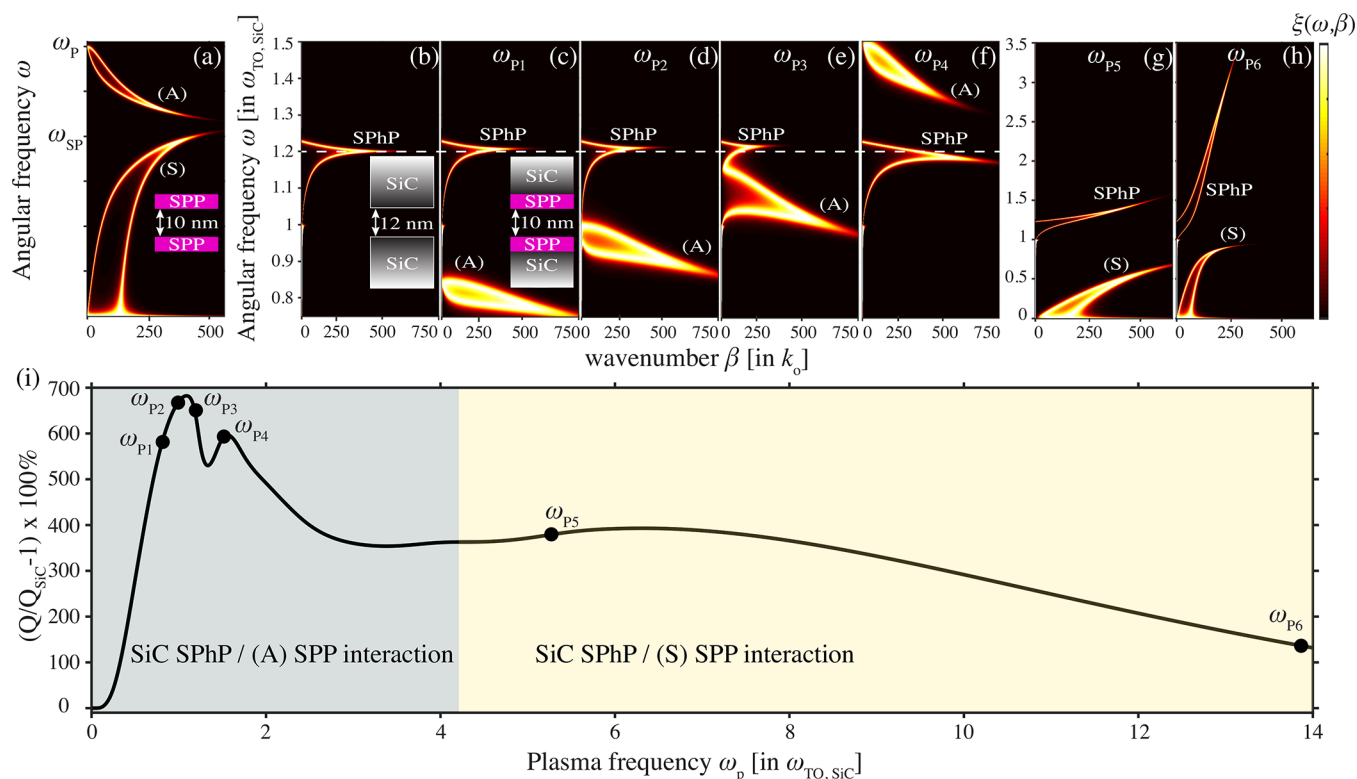
Figure 3. Near-field heat transfer between plasmonic thin films on SiC. (a) Photon transmission probability ξ for a pair of ultrathin plasmonic films separated by 10 nm, as depicted in the inset. Letters (A) and (S) refer to antisymmetric and symmetric electric field distribution with respect to the center of each plasmonic film. (b) Photon transmission probability for a pair of semi-infinite SiC slabs separated by a 12 nm vacuum gap, as depicted in the inset. (c−h) Photon transmission probabilities for a pair of plasmonic thin films of thickness 1 nm on SiC, separated by a 10 nm vacuum gap, as depicted in the inset of (c). The momentum-relaxation rate is set at $\gamma_p = 5\gamma_{SiC}$, while the plasma frequency is $\omega_{P1} = 0.85\omega_{TO,SiC}$ (c), $\omega_{P2} = \omega_{TO,SiC}$ (d), $\omega_{P3} = 1.15\omega_{TO,SiC}$ (e), $\omega_{P4} = 1.5\omega_{TO,SiC}$ (f), $\omega_{P5} = 5.5\omega_{TO,SiC}$ (g), and $\omega_{P6} = 14\omega_{TO,SiC}$ (h). (i) Total heat flux (relative to SiC) for the heterostructure in the inset of panel (c), for increasing ω_p of the plasmonic film, and for $T_1 = 600$ K and $T_2 = 300$ K. The gray-highlighted regime corresponds to the frequency range where the SiC SPhP interacts with the (A) branches of the SPP, and the relevant photon transmission probabilities are displayed in panels (c)−(f), whereas the yellow-highlighted regime corresponds to the interaction of the SiC SPhP with the (S) SPP branches, and the relevant transmission probabilities are in panels (g) and (h).

semi-infinite SiC plates, Q_{SiC}. In Figure 2a, we consider $\gamma_p = 5\gamma_{SiC}$, where $\gamma_{SiC} = 8.97 \times 10^{11}$ rad/s is the phonon relaxation rate in SiC, and consider various plasma frequencies. For each plasma frequency, we plot the photon transmission probability $\xi(\omega, \beta)$. The position of $\omega-\beta$ pairs where $\xi(\omega, \beta)$ reaches unity thus appears as a contour in the $\omega-\beta$ plane. In Figure 2a, the plasma frequency is set to $\omega_{P1} = 0.25\omega_{TO,SiC} \approx 8\gamma_p$ (lower curve), $\omega_{P2} = 1.5\omega_{TO,SiC} \approx 50\gamma_p$ (middle curve), and $\omega_{P3} = 4.5\omega_{TO,SiC} \approx 150\gamma_p$ (top curve). On each contour, the $\omega-\beta$ coordinates where the largest β occurs agree well with eq 7.

The analysis above on ω_{res}, in combination with the form of eq 1, points to the mechanisms through which changing of ω_p can influence the heat transfer. The spectral transfer function $S(\omega)$, as shown by the dashed lines in Figure 2b, for the same ω_p's as the ones considered in panel (a), peaks strongly near ω_{res}. Moreover, the peak value of $S(\omega)$ increases as a function of ω_p, due to the increase of β_{res} as discussed above. On the other hand, the energy exchange per photon, $\Theta(\omega, T_1) - \Theta(\omega, T_2)$, maximizes at $\omega = 0$ and gradually decreases as ω increases (red curve in Figure 2b). Consequently, the near-field heat flux Q between the two bodies increases with ω_p in the regime of small ω_p and decreases with ω_p in the regime of large ω_p, as shown by the black curve in Figure 2b. Since ω_p is directly related to the carrier concentration, the results here thus show that it is possible to drastically influence the near-field heat transfer in a plasmonic system by modulating the carrier density.

INTERACTION OF SURFACE PLASMON AND SURFACE PHONON POLARITON

In the previous section, we have shown that in a plasmonic system changing the plasma frequency can lead to substantial modulation and switching of near-field heat transfer. In practice, the thermal MOS switch, as shown in Figure 1, represents the most practical way to tune the plasma frequency of a heavily doped semiconductor layer. Compared with the idealized geometry as shown in the previous section, however, the thermal MOS switch in Figure 1 differs in two significant aspects: (i) The heavily doped region is of necessity a thin film, so that a modest voltage applied can lead to substantial change in the plasma frequency. (ii) There is a need for the oxide region for voltage gating purposes. As we will discuss in this section, both of these aspects significantly affect the characteristics of near-field heat transfer in the MOS configuration as compared to that between two bulk plasmonic regions.

We consider near-field heat transfer between a pair of plasmonic thin films first (inset in Figure 3a). The peaks of the photon transmission probability consist of two main branches, labeled with (S) and (A) in Figure 3a, each of which consists of two secondary branches. The labels (S) and (A) pertain to an electric field distribution that is symmetric and antisymmetric, respectively, with respect to the center of the plasmonic film, whereas within each main branch the lower (upper) frequency

secondary branch has a symmetric (antisymmetric) field distribution with respect to the center of the gap.

In Figure 3b, we consider a pair of semi-infinite SiC interfaces separated by a 12 nm vacuum gap. We model the permittivity of SiC with the Lorentz model,[52−54] $\epsilon_{SiC}(\omega) = \epsilon_\infty[(\omega_{LO}^2 - \omega^2 - i\gamma\omega)/(\omega_{TO}^2 - \omega^2 - i\omega\gamma)]$, where $\epsilon_{\infty,SiC} = 6.7$, $\omega_{LO,SiC} = 1.83 \times 10^{14}$ rad/s and $\gamma_{SiC} = 8.97 \times 10^{11}$ rad/s, $\omega_{TO,SiC} = 1.49 \times 10^{14}$ rad/s, as mentioned above. The transmission probability ξ reaches unity along the SPhP modes of the coupled SiC−vacuum interfaces. The frequency range $[1,1.2]\omega_{TO,SiC}$ of these modes is the SiC Reststrahlen band. β_{res} occurs near the frequency $\omega \sim 1.2\omega_{TO,SiC}$, where $\epsilon_{SiC} \approx -1$.

The characteristics of near-field heat transfer in the structure of Figure 1 can be understood in terms of the interaction between the bulk SiC SPhP modes with the plasmonic modes of the thin film. We start from the bulk SiC configuration and add two plasmonic films of thickness 1 nm atop SiC, so that the vacuum gap is now set at 10 nm, as shown in the inset of Figure 3c. The parameter ω_p of the plasmonic film is set to $\omega_{P1} = 0.85\omega_{TO,SiC}$, while γ_p remains at $5\gamma_{SiC}$ as in Figures 2 and 3a. Due to the low ω_p in Figure 3c, only the (A) SPP branch is visible, and the (S) branch lies at lower frequencies. The SPhP mode at the Reststrahlen band of SiC is not affected by the (A) SPP mode. By increasing the plasma frequency to $\omega_{P2} = \omega_{TO,SiC}$, the (A) SPP mode blue-shifts (Figure 3d) until, at $\omega_{P3} = 1.15\omega_{TO,SiC}$, the SiC SPhP mode overlaps in frequency with the (A) SPP (Figure 3e). We note that even though the bands overlap, the shapes of the SPhP modes and the SPP modes remain largely unchanged, indicating the weak interaction between the (A) SPP branch and the SPhP modes. Increasing the plasma frequency further, to $\omega_{P4} = 1.5\omega_{TO,SiC}$, blue-shifts the (A) SPP mode to frequencies beyond the Reststrahlen band of SiC (Figure 3f).

Figure 3i displays the enhancement in total integrated near-field heat transfer, Q, of the plasmonic film on SiC (inset in Figure 3c) with respect to bulk SiC (inset in Figure 3b), as a function of ω_p. The regime of $\omega_p < 4\omega_{TO,SiC}$, highlighted with gray, corresponds to the plots discussed above (panels (c)−(f)), for which the SiC SPhP overlaps with the (A) SPP branch. It can be seen that by placing an ultrathin plasmonic film on SiC one can enhance the net near-field heat transfer by almost 700%, by appropriately positioning the plasma frequency ω_p with respect to $\omega_{TO,SiC}$. This enhancement is the result of an additional channel for transferring heat, namely, the (A) SPP branch, aside from the fundamental SPhP channel of SiC. The dip in Q at $\omega_p \approx 1.3\omega_{TO,SiC}$ identifies the point at which the (A) SPP mode crosses over the Reststrahlen band of SiC[66] (Figure 3e,f).

In contrast to the near-field heat transfer, $Q(\omega_p)$, of the bulk case, which exhibits a single maximum as a function of ω_p (Figure 2b), a pair of thin plasmonic films on SiC supports an additional local maximum at high $\omega_p > 4\omega_{TO}$, shown in the yellow-highlighted regime in Figure 3i. This second local maximum originates from the symmetric (S) SPP branch (see Figure 3a) interacting with the SiC SPhP and is more broadband in nature. In panels (g) and (f) we display the photon transmission probability relevant to this regime, particularly for $\omega_{P5} = 5.5\omega_{TO,SiC}$ and $\omega_{P6} = 14\omega_{TO,SiC}$. In contrast to panels (c)−(f), there is significant interaction between the SiC SPhP with the (S) SPP branch. This response is previously seen in heterostructures involving polaritonic materials and graphene, as the monolayer nature of graphene eliminates the (A) SPP mode and only the (S) SPP interacts with SPhPs.[23,40,67−70]

■ PRACTICAL IMPLEMENTATION

In Figure 3 we demonstrated that an ultrathin plasmonic film on SiC may significantly enhance near-field heat transfer with respect to bulk SiC. Furthermore, we showed that changes in the plasma frequency ω_p of the plasmonic film can tune near-field heat transfer considerably. Changes in ω_p may be induced via modulation of charge carrier density. In search for substances with tunable carrier density, we resort to three classes of materials: TCOs and nitrides, doped semiconductors, and graphene.

In the class of TCOs we investigate indium tin oxide (ITO), which is traditionally used as a contact electrode in photovoltaic cells due to its simultaneous conducting and transparent nature. ITO is an emerging plasmonic material with considerably lower losses compared to noble metals, while also having gate-tunable carrier density.[68,69,71−75] In the class of semiconductors we study Si,[70] as it is the most broadly used semiconductor in solid-state technology, ranging from solar harvesting to optoelectronics and silicon photonics. Graphene's monolayer thickness makes it an attractive candidate material for ultracompact near-field heat transfer thermal switches. The carrier density of these materials may be actively modulated when electrostatically gated, as described in the general concept of Figure 1, where they can be seen as the "S" of the thermal MOS switch. Below the active material lies a thick layer of SiC, which serves as the "oxide" of the thermal MOS switch. The SiC layer can sustain large gate voltages due to its large breakdown field of $E_{br} = 3$ MV/cm,[57−60] while also by itself contributing significantly to the heat transfer properties of the system, as we see in the previous section.[1,3,10−13,52−56] We set the thickness of the SiC layer to $\Delta = 1$ μm for ensuring that (i) the SiC SPhP behaves like the bulk SPhP discussed in Figure 3 and that (ii) large gate biases, V_g, may be applied prior to electrical breakdown occurring. We consider silver as the back-side gating electrode ("M" of the thermal MOS switch in Figure 1).

A. Transparent Conductive Oxides. We model ITO with the Drude model of eq 4, using $m^* = 0.35m_e$, $\gamma_p = 1.4 \times 10^{14}$ rad/s, and $\epsilon_\infty = 3.9$.[49,69,71,72,76] In Figure 4a we display the active (red) and background regions (yellow) of ITO. When no bias is applied ($V_g = 0$), the active and background regions have the same carrier density, $N_A = N_B$. An applied bias V_g causes accumulation ($N_A > N_B$) or depletion ($N_A < N_B$) of charge carriers in the active region, for which the plasma frequency ω_p blue-shifts and red-shifts, respectively. The thickness of the active region is defined by the Thomas−Fermi screening theory[69,76] and, to first order, can be approximated by the Debye length:[49,77]

$$L_D = \sqrt{\frac{\epsilon_o \epsilon_{o,SiC} k_B T}{e N_A}} \tag{8}$$

In eq 8 $\epsilon_{o,SiC}$ is the dc dielectric constant of SiC set to 9.72,[78] k_B is the Boltzmann constant, and T is the temperature. The active region is typically ultrathin, as shown for ITO at different carrier densities and temperatures in Figure 4b, i.e., on the order of 1−5 nm,[69,71,76] compared to the wavelength of thermal radiation that lies in the regime of tens of micrometers. Despite the minuscule size of the Debye length, small changes to its optical properties (ω_p) via carrier density modulation can significantly impact near-field heat transfer. By minimizing the thickness of the background region in Figure 4a, we maximize the range of tunability of near-field heat transfer by bringing the active region where changes of the optical properties take place
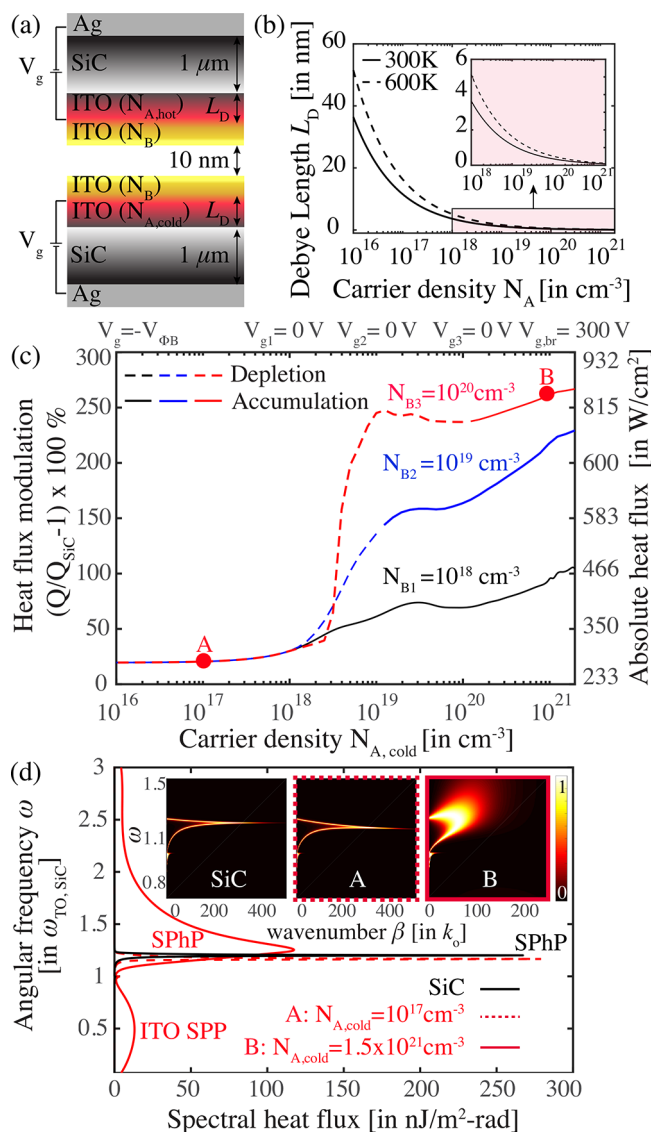
Figure 4. Practical implementation of a thermal MOS switch with ITO. (a) Schematic of ITO-based thermal MOS switch. (b) Debye length for ITO at different temperatures. (c) Total heat transfer coefficient for T_1 = 600 K and T_2 = 300 K, relative to the SiC benchmark, with respect to the carrier density $N_{A,cold}$ at the cold side. The background carrier density is $N_B = 10^{18}$, 10^{19}, and 10^{20} cm^{-3} in results shown with black, blue, and red, respectively. Positive V_g corresponds to accumulation ($N_A > N_B$, solid lines), and negative V_g corresponds to depletion ($N_A < N_B$, dashed lines). The maximum considered carrier density corresponds to the breakdown condition of SiC, $V_{g,br}$ = 300 V. The blackbody limit lies at $(Q/Q_{SiC} - 1) \times 100\%$ = −99.7%. (d) Spectral heat flux for carrier densities corresponding to points A and B in panel (c), in depletion and accumulation mode, respectively. Corresponding photon transmission probabilities are shown in the insets in depletion (middle) and accumulation (right). Results are compared to bulk SiC (black curve and leftmost inset).

as close to the vacuum gap as possible. SPPs and SPhPs that carry thermal energy across the vacuum gap (see Figure 1) are strongly confined in the vicinity of the vacuum gap/active material interface and are, therefore, highly sensitive to changes of the optical properties of this region. Here, we set the total thickness of the ITO layer (background and active region in Figure 4a) to 3 nm. The vacuum gap has a thickness d = 10 nm,

at which the framework of fluctuational electrodynamics holds accurately.[79,80]

The maximum achievable carrier density in the active region is subject to the SiC breakdown constraint through

$$\frac{V_g}{\Delta} = \frac{q_A}{\epsilon_o \epsilon_{o,SiC}} \leq E_{br} \qquad (9)$$

where q_A is the charge per area given by $q_A = e N_A L_D$. From eq 9 we compute the maximum carrier density, beyond which SiC cannot sustain the applied electric field. The corresponding breakdown voltage is $V_{g,br} = E_{br}\Delta$ = 300 V. We note, however, that as seen in the results that follow, heat flux is maximally tuned at a gate voltage considerably smaller than $V_{g,br}$; therefore one does not need to operate near the breakdown point of the MOS's oxide, where leakage issues may arise. Furthermore, the magnitude of $V_{g,br}$ scales with the thickness of the oxide; therefore, for applications that require a small gate voltage, a thinner oxide with larger E_{br} may be more suitable than SiC, such as SiO$_2$ or HfO$_2$.[49]

The minimum considered carrier density corresponds to the flat band condition $V_g = -V_{\Phi B}$, which sets the boundary between operation in inversion and depletion mode in an MOS.[77] For V_g in the range $[-V_{\Phi B}, 0]$, majority carriers, i.e., electrons for ITO, are depleted in the active region, and its optical response becomes more dielectric compared to the background. By contrast, for V_g in the range $[0, V_{g,br}]$, majority carriers are accumulated in the active region, which becomes more metallic with respect to the background. Operation in inversion mode ($V_g < -V_{\Phi B}$) is not considered here, as it affects near-field heat transfer in the same way as in accumulation mode, with the role of majority carriers inverted.

The total calculated heat transfer, Q, as a function of the carrier density in the active region is shown in Figure 4c. Q is plotted normalized to the heat exchange between a pair of semi-infinite SiC surfaces separated by 16 nm, Q_{SiC}, i.e., in the absence of the ITO thin films, whereas on the right vertical axis absolute values of power density are also displayed. The considered background carrier densities are $N_B = 10^{18}$, 10^{19}, and 10^{20} cm^{-3}, shown with black, blue, and red, respectively. Depletion mode is depicted with dashed lines, whereas accumulation mode is depicted with solid lines. As seen at $V_g = V_{g,br}$, near-field heat transfer is maximized for maximum carrier density in the background region, namely, for $N_B = 10^{20}$ cm^{-3}. This result is expected as explained in detail in Figures 2 and 3; increasing carrier density, and therefore increasing ω_p, leads to an increase in total near-field heat transfer, contributed by the SPP channel, as long as the mean energy exchange per photon overlaps with the SPP resonance frequency.

In Figure 4c we demonstrated that adding an ultrathin plasmonic film of ITO on SiC can induce significant enhancement to the neat heat transfer with respect to bulk SiC. Importantly, we showed that field effect modulation of the carrier density leads to active control of near-field heat transfer, which can vary with respect to SiC between 20% and 265%. By considering the OFF and ON states of this near-field heat transfer modulating scheme to correspond to $V_g = 0$ V and $V_g = V_{g,br}$ = 300 V, respectively, we obtain contrast ratios as high as 190%.

In Figure 4d we display the spectral heat flux, defined as the integrant quantity in eq 1, with respect to bulk SiC, as discussed in panel (c). Results are shown for depletion (dashed lines) and accumulation (solid lines), corresponding to the points A and B

in panel (c), respectively. The spectral heat flux for bulk SiC is shown with the black curve for comparison. Additionally, in the insets are the photon transmission probabilities (ξ) for bulk SiC (left) as well as for depletion (middle) and accumulation (right) modes of our system with ITO. In the depletion mode, the photon transmission probability and respective heat flux do not change considerably with respect to bulk SiC. This is explained by the low carrier density at point A in Figure 4c that yields small ω_p with respect to $\omega_{TO,SiC}$; therefore the SPP of ITO is too low in frequency to strongly interact with the Reststrahlen band of SiC or to contribute significantly to heat transfer. The slight increase in integrated heat flux at point A, with respect to bulk SiC, in Figure 4c, results from the large plasmonic losses (γ_p) in ITO, namely, $\gamma_{ITO} = [200-263]\gamma_{SiC}$,[49,68,69,71,72,76] for the range of carrier densities considered here. The ITO losses result in a slightly broadened SPhP peak in spectral heat flux (dashed curve in panel (d)) with respect to bulk SiC (black curve in panel (d)), which, when integrated, results in a Q larger than Q_{SiC}.

In the accumulation mode, the ITO SPP branch blue-shifts considerably, resulting in an additional broad peak in spectral heat flux, noted as ITO SPP in panel (d) of Figure 4 (solid red curve). The broadband nature of the ITO SPP peak is also the result of large plasmonic losses in ITO, which makes it hard to distinguish it from the SiC SPhP in the photon transmission probability on the right-side inset of Figure 4d.

B. Doped Semiconductors. Next, we consider p-doped Si as the active material, in a configuration identical to that of Figure 4a, where ITO is replaced by Si. We model doped Si with ref 70, accounting for temperature effects on the dielectric function, namely, on the effective mass of holes and electrons m^*, the momentum-relaxation rate γ_p, and band gap. The total calculated heat transfer, Q, is shown in Figure 5a, where dashed lines correspond to operation in the depletion mode, whereas solid lines correspond to the accumulation mode. In contrast to the system with ITO in Figure 4, here, since Si is p-doped, accumulation and depletion correspond to increase and decrease in the number of holes as majority carriers in the active region, with respect to the background, respectively. With respect to bulk SiC, near-field heat transfer can vary between −12% and 185%. The ON ($V_g = 0$ V)/OFF ($V_g = V_{g,br} = 300$ V) contrast ratio achievable with p-doped Si can be as high as 225%, in contrast to 190% with ITO (Figure 4). This increase in contrast ratio arises because, in depletion mode and for small carrier densities, p-doped Si on SiC suppresses near-field heat transfer ($Q < Q_{SiC}$), in contrast to ITO. This suppression in near-field heat transfer stems from the strong temperature dependence of the dielectric function of Si.[70] Specifically, when the dielectric functions of the hot and cold sides differ considerably, the thermally excited SPPs from the two sides do not couple efficiently. For instance, there exist regimes of frequencies and carrier densities for which the dielectric functions of p-Si at temperatures T_1 and T_2 may be opposite in sign; hence the SPPs thermal channel is eliminated. Exploiting this effect, the contrast ratio (ON/OFF) of near-field heat transfer can be further enhanced by spectrally misaligning the surface plasmonic resonances of the cold and hot sides of the thermal MOS (Figure 1 and Figure 7a).

In Figure 5b we display the spectral heat flux and corresponding photon transmission probability ξ for points A and B, corresponding to the accumulation and depletion modes in Figure 5a, respectively. Similar to the ITO system discussed previously, we note that the large plasmonic losses (γ_p) of Si, namely, $\gamma_{Si} = [26-223]\gamma_{SiC}$ for the range of temperatures and
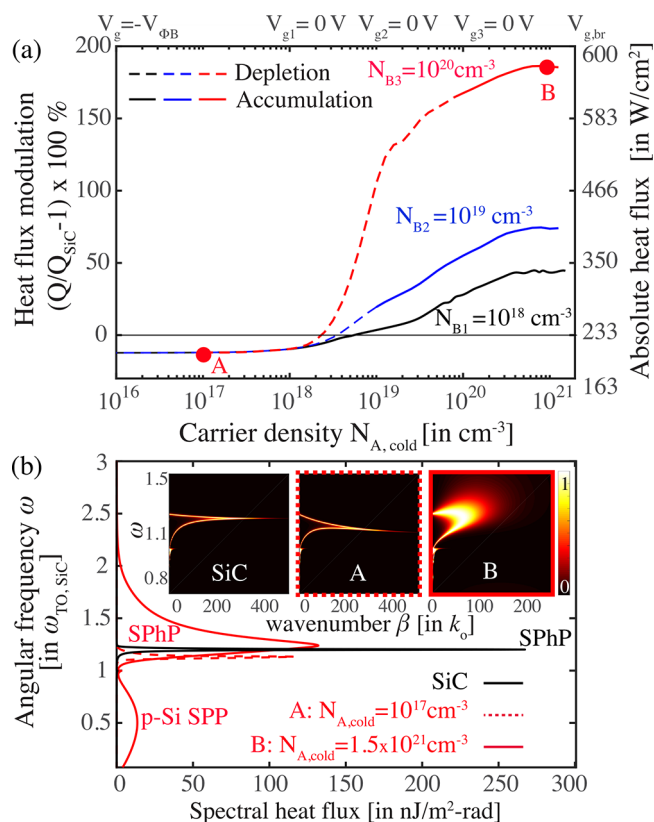

Figure 5. Thermal MOS switch with p-doped Si. (a) Total heat transfer coefficient for $T_1 = 600$ K and $T_2 = 300$ K, relative to the SiC benchmark, with respect to the carrier density $N_{A,cold}$ at the cold side. The background carrier density is $N_B = 10^{18}$, 10^{19}, and 10^{20} cm^{-3} in results shown with black, blue, and red, respectively. The blackbody limit lies at $(Q/Q_{SiC} - 1) \times 100\% = -99.7\%$. (b) Spectral heat flux for carrier densities corresponding to points A and B in panel (a), in depletion and accumulation mode, respectively. Corresponding photon transmission probabilities are shown in the insets in depletion (middle curve) and accumulation (right curve). Results are compared to bulk SiC (black curve and leftmost ξ curve).

carrier densities considered here,[70] strongly perturb the dispersion of the SiC SPhP when interacting with the p-Si SPP, which makes them hard to distinguish in the plot for ξ in the accumulation mode (right panel).

C. Graphene. Finally, we consider the system consisting of a graphene sheet on SiC, in the configuration shown in the inset of Figure 6a, where we account for the monolayer by setting the thickness of graphene to $L_g = 0.33$ nm, which is the interlayer separation distance of graphite.[40,67,81] For the sake of comparison with the ITO and doped Si cases examined previously, we set the vacuum gap thickness to $d = 16$ nm in order to maintain the same distance between the SiC interfaces for all three examined materials. We model graphene with the Drude model, by first computing its optical conductivity, which connects to permittivity via $\epsilon_g(\omega) = 1 + i\sigma/(\epsilon_o \omega L_g)$, while taking into account the temperature dependence of both interband and intraband contributions.[40,82] The charge carrier density $N_{graphene}$ and Fermi level E_F are connected via $E_F = \hbar|v_F|\sqrt{\pi N_{graphene}}$,[38,81] where v_F is the Fermi velocity. We take into account the effect of gating on the Fermi velocity and momentum-relaxation rate γ_p, following ref 81.

In determining the maximum achievable doping and corresponding Fermi level in graphene, the charge per area, q_A
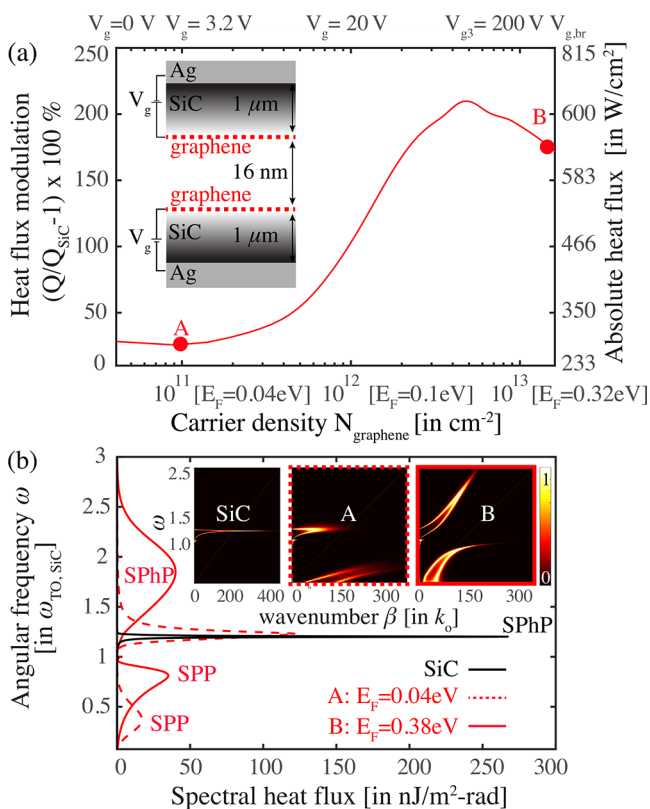
Figure 6. Thermal MOS switch with graphene. (a) Total heat transfer coefficient for $T_1 = 600$ K and $T_2 = 300$ K, relative to the SiC benchmark, with respect to the carrier density N_{graphene} and corresponding Fermi level E_F. Top horizontal axis is the required applied bias V_g for obtaining the corresponding heat flux. The maximum considered carrier density corresponds to the breakdown condition of SiC, i.e., $V_{g,\text{br}} = 300$ V. The blackbody limit lies at $(Q/Q_{\text{SiC}} - 1) \times 100\% = -99.7\%$. (b) Spectral heat flux for carrier densities corresponding to points A and B in panel (a), shown with dashed and solid red curves, respectively. Corresponding photon transmission probabilities are shown in the insets. Results are compared to bulk SiC (black curve and leftmost ξ curve).

in eq 9, is given by $q_A = eN_{\text{graphene}}$, where N_{graphene} has units of m^{-2}. The minimum considered carrier density in graphene is $N_{\text{graphene}} = 0$, which corresponds to Fermi level $E_F = 0$ eV and to $V_g = 0$ V. Extending the range of considered applied bias to $V_g = [-V_{g,\text{br}}, 0]$, i.e., inverting the role of electrons and holes, would yield the same near-field heat transfer $(Q(V_g))$ as for $V_g > 0$, due to linear electronic dispersion of graphene based on which electrons and holes affect its optical properties on equal footing.

In Figure 6a we show the total heat transfer, Q, normalized to SiC, as a function of the carrier density. The brackets in the horizontal axis indicate the corresponding Fermi level, E_F, with respect to the charge neutrality point $(N_{\text{graphene}} = 0)$. The top horizontal axis provides estimates for the gate voltage V_g required for obtaining the corresponding near-field heat transfer rate. With respect to bulk SiC, the addition of a monolayer sheet of graphene with tunable carrier density yields a near-field heat transfer modulation that varies between 25% and 200%. The maximum contrast (ON/OFF) ratio is 147%, and maximum heat transfer occurs at a Fermi level of approximately 0.2 eV. Figure 6b displays the spectral heat flux corresponding to points A (dashed red curve) and B (solid red curve) in panel (a), i.e., for low and high E_F, respectively, in addition to the spectral heat flux for bulk SiC (black curve). At $E_F = 0.04$ eV, we observe two

peaks in spectral heat flux, one arising from the SiC SPhP, which lies at $\omega = 1.2\omega_{\text{TO,SiC}}$, and one due to graphene's SPP, near $\omega = 0.2\omega_{\text{TO,SiC}}$, while the corresponding photon transmission probability is shown in the middle inset. The slight blue-shift of the SPhP resonance with respect to the bulk SiC case (black line) results from band repulsion, discussed in Figure 3. Increasing the Fermi level to $E_F = 0.38$ eV broadens the SPhP peak due to band flattening, as is shown with the photon transmission probability in the rightmost inset. Compared to the cases of ITO (Figure 4) and p-doped Si (Figure 5), plasmonic losses in graphene are reduced by 2 orders of magnitude,[38,40,81,82] making the graphene SPP mode easily distinguishable from the SiC SPhP mode in the plots of photon transmission probability shown in the insets in Figure 6b.

In a practical realization of the thermal MOS, one may choose to gate both hot and cold sides as discussed previously or, for the sake of simplicity, operate a single-gated motif as the one shown in the inset of Figure 7a. We consider this case using the graphene-based heterostructure discussed above, because graphene's lower optical losses allow highlighting the underlying physics better than by considering the doped Si or ITO heterostructures. Conclusions drawn here hold equally for doped Si and ITO. We consider gating the hot side of the
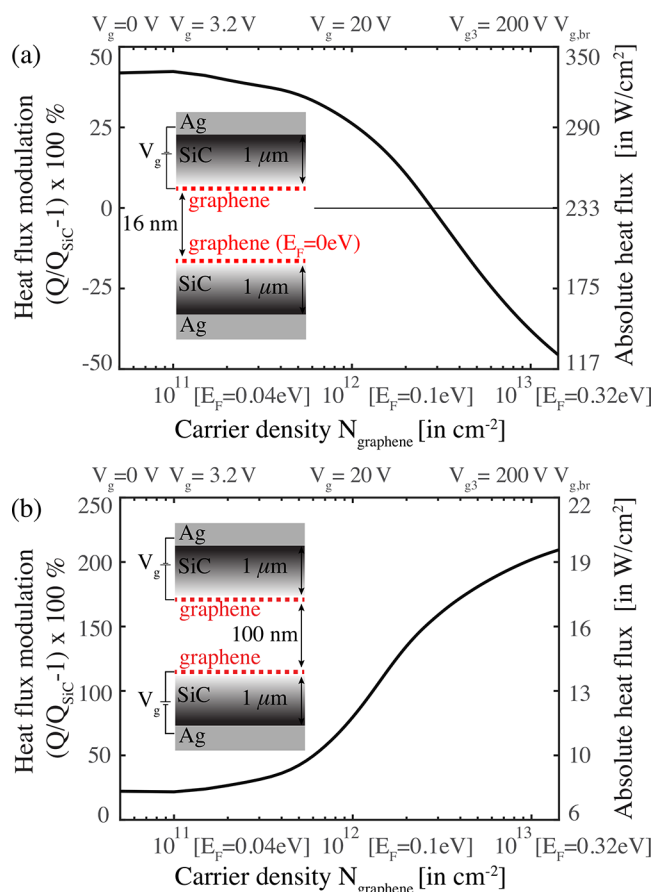

Figure 7. Single-gated thermal MOS and increased vacuum gap size. (a) Total heat transfer coefficient for the structure and parameters of Figure 6, for a single-gated thermal MOS, where the cold side ($T_2 = 300$ K) is kept at 0 V, whereas the hot side ($T_2 = 600$ K) is gated. The horizontal axis pertains to the carrier density and Fermi level of the hot side's gated graphene sheet. (b) Total heat transfer coefficient for the structure and parameters of Figure 6 for a larger vacuum gap size of $d = 100$ nm.

thermal MOS, which remains at $T_1 = 600$ K, while maintaining the cold side at $T_2 = 300$ K, and its graphene is set at $E_{F,cold} = 0$ eV (inset in Figure 7a). In Figure 7a we display the computed near-field heat transfer with respect to SiC, as previously. At a small gate voltage, the total heat flux increases with respect to SiC by approximately 43%. This is expected because the difference between the two graphene sheets' Fermi levels $\Delta E_F = E_{F,hot} - E_{F,cold}$ is small; therefore the hot and cold side SPP channels are close in resonance frequency and, hence, transfer heat efficiently. By contrast, however, to the results pertaining to a double-gated structure (Figure 6a), where increasing the gate voltage monotonically increases the heat flux, a single-gated motif yields the opposite trend and is able to suppress the heat flux with respect to bulk SiC, as shown for large E_F in Figure 7a. This is anticipated as, in this case, the SPP resonance frequency of the plasmon at the hot side of the thermal MOS is significantly shifted with respect to that of the cold side's SPP ($E_{F,cold} = 0$ eV); therefore the two SPP channels do not overlap sufficiently in frequency for efficiently transferring heat. Figure 7a shows that a single-gated structure suffices for tuning heat transfer to ratios ±50% with respect to SiC.

Another practical issue is that of the vacuum gap size, which was previously set to $d = 10$ nm. Here we carry out the calculation for the graphene-based thermal MOS discussed in Figure 6 for a larger vacuum gap size of $d = 100$ nm (see inset in Figure 7b), a value that has been previously achieved experimentally.[61,80,83] As seen in Figure 7b, the contrast ratio in heat transfer does not change considerably, in comparison to Figure 6a. This arises since the contrast ratio quantifies the change in heat transfer with respect to two bulk SiC surfaces separated by the same vacuum gap size, and the SPP channels hosted at the hot and cold sides of the graphene-based thermal MOS experience similar changes in their respective resonance frequencies due to gating, regardless of their separation distance. Nevertheless, the absolute value of power density is considerably decreased as the separation distance increases, obeying the $1/d^3$ dependence discussed in previous work.[1,11] Particularly, two bulk SiC interfaces at $d = 10$ nm exchange a heat flux of 233 W/cm² (Figures 4−6); however when separated by $d = 100$ nm, they exchange a heat flux of 6 W/cm² (Figure 7b). Similar conclusions can be drawn for the ITO- and p-doped Si-based thermal MOS discussed previously.

CONCLUSIONS

In conclusion, we proposed a thermal MOS switch for active modulation of heat flux in the near-field, as a counterpart to the electronic MOS transistor. The proposed idea stems from the same physical principle of operation as the field effect transistor, namely, the accumulation and depletion of charge carriers in an active material electrostatically gated against a back electrode. The near-field heat transfer modulation speed is, therefore, the same as the modulation rate of the field effect, which lies in the GHz range.[47,48] For modulation speeds up to tens of MHz, the calculations for the proposed implementations here hold accurately without modification to the estimated gate voltage for tuning heat transfer, while small corrections to the maximum breakdown voltage may be in order for faster modulation rates. Furthermore, the proposed module can be compatible with current CMOS technology. By performing photonic calculations of near-field heat transfer, while taking into account electrostatic considerations, we showed that by accumulation and depletion of charge carriers in ultrathin layers of ITO and doped Si, and in monolayer graphene, on SiC, contrast ratios as large as 225%

may be achieved. The required gate voltage for modulation is determined by the breakdown field of the material that serves as the oxide in the MOS scheme. SiC is optimal for tunable near-field heat transfer via electrostatic gating due to its good insulating properties, in addition to its pronounced SPhP resonance that optimally transfers heat in the near-field at moderate temperatures. Our results demonstrate the possibility of actively controlling heat flux in the near-field, in a platform adoptable in modern optoelectronics, hence targeting applications in thermal cooling, recycling, and thermal circuitry.

METHODS

The computational package used for near-field heat transfer calculations can be found in ref 84.

AUTHOR INFORMATION

Corresponding Author
*E-mail: shanhui@stanford.edu.

ORCID ⊕
Georgia T. Papadakis: 0000-0001-8107-9221
Bo Zhao: 0000-0002-3648-6183

Notes
The authors declare no competing financial interest.

REFERENCES

(1) Shchegrov, A. V.; Joulain, K.; Carminati, R.; Greffet, J.-J. Near-field spectral effects due to electromagnetic surface excitations,. *Phys. Rev. Lett.* **2000**, *85*, 1548−1551.

(2) Laroche, M.; Carminati, R.; Greffet, J.-J. Near-field thermophotovoltaic energy conversion,. *J. Appl. Phys.* **2006**, *100* (6), 063704.

(3) Mulet, J.-P.; Joulain, K.; Carminati, R.; Greffet, J.-J. Enhanced radiative heat transfer at nanometric distances,. *Microscale Thermophys. Eng.* **2002**, *6* (3), 209−222.

(4) Fan, S. Thermal photonics and energy applications,. *Joule* **2017**, *1* (2), 264−273.

(5) Li, W.; Fan, S. Nanophotonic control of thermal radiation for energy applications,. *Opt. Express* **2018**, *26* (12), 15995−16021.

(6) Greffet, J.-J.; Carminati, R.; Joulain, K.; Mulet, J.-P.; Mainguy, S.; Chen, Y. Coherent emission of light by thermal sources,. *Nature* **2002**, *416*, 61−64.

(7) Liu, X.; Tyler, T.; Starr, T.; Starr, A. F.; Jokerst, N. M.; Padilla, W. J. Taming the blackbody with infrared metamaterials as selective thermal emitters,. *Phys. Rev. Lett.* **2011**, *107*, 045901.

(8) Yeng, Y. X.; Ghebrebrhan, M.; Bermel, P.; Chan, W. R.; Joannopoulos, J. D.; Soljačić, M.; Celanovic, I. Enabling high-temperature nanophotonics for energy applications,. *Proc. Natl. Acad. Sci. U. S. A.* **2012**, *109* (7), 2280−2285.

(9) De Zoysa, M.; Asano, T.; Mochizuki, K.; Oskooi, A.; Inoue, T.; Noda, S. Conversion of broadband to narrowband thermal emission through energy recycling,. *Nat. Photonics* **2012**, *6*, 535.

(10) Jones, A. C.; O'Callahan, B. T.; Yang, H. U.; Raschke, M. B. The thermal near-field: Coherence, spectroscopy, heat-transfer, and optical forces,. *Prog. Surf. Sci.* **2013**, *88* (4), 349−392.

(11) Basu, S.; Zhang, Z. M.; Fu, C. J. Review of near-field thermal radiation and its application to energy conversion,. *Int. J. Energy Res.* **2009**, *33* (13), 1203−1232.

(12) Joulain, K.; Mulet, J.-P.; Marquier, F.; Carminati, R.; Greffet, J.-J. Surface electromagnetic waves thermally excited: Radiative heat transfer, coherence properties and casimir forces revisited in the near field,. *Surf. Sci. Rep.* **2005**, *57* (3), 59−112.

(13) St-Gelais, R.; Zhu, L.; Fan, S.; Lipson, M. Near-field radiative heat transfer between parallel structures in the deep subwavelength regime,. *Nat. Nanotechnol.* **2016**, *711* (1), 515.

(14) Ben-Abdallah, P.; Biehs, S.-A. Near-field thermal transistor,. *Phys. Rev. Lett.* **2014**, *112*, 044301.

(15) Li, B.; Wang, L.; Casati, G. Negative differential thermal resistance and thermal transistor,. *Appl. Phys. Lett.* **2006**, *88* (14), 143501.

(16) Zhao, B.; Chen, K.; Buddhiraju, S.; Bhatt, G.; Lipson, M.; Fan, S. High-performance near-field thermophotovoltaics for waste heat recovery,. *Nano Energy* **2017**, *41*, 344−350.

(17) Karalis, A.; Joannopoulos, J. D. Squeezing near-field thermal emission for ultra-efficient high-power thermophotovoltaic conversion. *Sci. Rep.* **2016**, *6*, 28472.

(18) Park, K.; Basu, S.; King, W.; Zhang, Z. Performance analysis of near-field thermophotovoltaic devices considering absorption distribution,. *J. Quant. Spectrosc. Radiat. Transfer* **2008**, *109* (2), 305−316 The Fifth International Symposium on Radiative Transfer. .

(19) Khandekar, C.; Messina, R.; Rodriguez, A. W. Near-field refrigeration and tunable heat exchange through four-wave mixing,. *AIP Adv.* **2018**, *8* (5), 055029.

(20) Kittel, A.; Wischnath, U. F.; Welker, J.; Huth, O.; Rting, F.; Biehs, S.-A. Near-field thermal imaging of nanostructured surfaces,. *Appl. Phys. Lett.* **2008**, *93* (19), 193109.

(21) De Wilde, Y.; Formanek, F.; Carminati, R.; Gralak, B.; Lemoine, P.-A.; Joulain, K.; Mulet, J.-P.; Chen, Y.; Greffet, J.-J. Thermal radiation scanning tunnelling microscopy,. *Nature* **2006**, *444*, 740.

(22) Shockley, W. A Unipolar Field-Effect Transistor. *Proc. IRE* **1952**, *40*, 473−484.

(23) Engelbrecht, S. G.; Reichel, A. J.; Kersting, R. Charge carrier relaxation and effective masses in silicon probed by terahertz spectroscopy,. *J. Appl. Phys.* **2012**, *112* (12), 123704.

(24) van Zwol, P. J.; Joulain, K.; Ben Abdallah, P.; Greffet, J. J.; Chevrier, J. Fast nanoscale heat-flux modulation with phase-change materials,. *Phys. Rev. B: Condens. Matter Mater. Phys.* **2011**, *83*, 201404.

(25) Qazilbash, M. M.; Brehm, M.; Chae, B.-G.; Ho, P.-C.; Andreev, G. O.; Kim, B.-J.; Yun, S. J.; Balatsky, A. V.; Maple, M. B.; Keilmann, F.; Kim, H.-T.; Basov, D. N. Mott transition in vo2 revealed by infrared spectroscopy and nano-imaging. *Science* **2007**, *318* (5857), 1750−1753.

(26) van Zwol, P. J.; Joulain, K.; Ben-Abdallah, P.; Chevrier, J. Phonon polaritons enhance near-field thermal transfer across the phase transition of vo$_2$,. *Phys. Rev. B: Condens. Matter Mater. Phys.* **2011**, *84*, 161413.

(27) Dyakov, S. A.; Dai, J.; Yan, M.; Qiu, M. Near field thermal memory based on radiative phase bistability of vo 2,. *J. Phys. D: Appl. Phys.* **2015**, *48* (30), 305104.

(28) Menges, F.; Dittberner, M.; Novotny, L.; Passarello, D.; Parkin, S. S. P.; Spieser, M.; Riel, H.; Gotsmann, B. Thermal radiative near field transport between vanadium dioxide and silicon oxide across the metal insulator transition,. *Appl. Phys. Lett.* **2016**, *108* (17), 171904.

(29) Ito, K.; Nishikawa, K.; Miura, A.; Toshiyoshi, H.; Iizuka, H. Dynamic modulation of radiative heat transfer beyond the blackbody limit,. *Nano Lett.* **2017**, *17* (7), 4347−4353.

(30) Huang, Y.; Boriskina, S. V.; Chen, G. Electrically tunable near-field radiative heat transfer via ferroelectric materials,. *Appl. Phys. Lett.* **2014**, *105* (24), 244102.

(31) Abraham Ekeroth, R. M.; Ben-Abdallah, P.; Cuevas, J. C.; Garca-Martn, A. Anisotropic thermal magnetoresistance for an active control of radiative heat transfer,. *ACS Photonics* **2018**, *5* (3), 705−710.

(32) Moncada-Villa, E.; Fernández-Hurtado, V.; García-Vidal, F. J.; García-Martín, A.; Cuevas, J. C. Magnetic field control of near-field radiative heat transfer and the realization of highly tunable hyperbolic thermal emitters,. *Phys. Rev. B: Condens. Matter Mater. Phys.* **2015**, *92*, 125418.

(33) Ben-Abdallah, P. Photon thermal hall effect,. *Phys. Rev. Lett.* **2016**, *116*, 084301.

(34) Zhu, L.; Fan, S. Persistent directional current at equilibrium in nonreciprocal many-body near field electromagnetic heat transfer,. *Phys. Rev. Lett.* **2016**, *117*, 134303.

(35) Latella, I.; Ben-Abdallah, P. Giant thermal magnetoresistance in plasmonic structures,. *Phys. Rev. Lett.* **2017**, *118*, 173902.

(36) Kou, J.; Minnich, A. J. Dynamic optical control of near-field radiative transfer,. *Opt. Express* **2018**, *26* (18), A729−A736.

(37) Khandekar, C.; Messina, R.; Rodriguez, A. W. Near-field refrigeration and tunable heat exchange through four-wave mixing,. *AIP Adv.* **2018**, *8* (5), 055029.

(38) Ilic, O.; Jablan, M.; Joannopoulos, J. D.; Celanovic, I.; Buljan, H.; Soljačić, M. Near-field thermal radiation transfer controlled by plasmons in graphene,. *Phys. Rev. B: Condens. Matter Mater. Phys.* **2012**, *85*, 155422.

(39) Ilic, O.; Thomas, N. H.; Christensen, T.; Sherrott, M. C.; Soljačić, M.; Marin; Minnich, A. J.; Miller, O. D.; Atwater, H. A. Active radiative thermal switching with graphene plasmon resonators,. *ACS Nano* **2018**, *12* (3), 2474−2481.

(40) Zhao, B.; Guizal, B.; Zhang, Z. M.; Fan, S.; Antezza, M. Near-field heat transfer between graphene/hbn multilayers,. *Phys. Rev. B: Condens. Matter Mater. Phys.* **2017**, *95*, 245437.

(41) Lim, M.; Lee, S. S.; Lee, B. J. Near-field thermal radiation between graphene-covered doped silicon plates,. *Opt. Express* **2013**, *21* (19), 22173−22185.

(42) Hong, X.-J.; Wang, T.-B.; Zhang, D.-J.; Liu, W.-X.; Yu, T.-B.; Liao, Q.-H.; Liu, N.-H. The near-field radiative heat transfer between graphene/sic/hbn multilayer structures,. *Mater. Res. Express* **2018**, *5* (7), 075002.

(43) Messina, R.; Ben-Abdallah, P.; Guizal, B.; Antezza, M. Graphene-based amplification and tuning of near-field radiative heat transfer between dissimilar polar materials,. *Phys. Rev. B: Condens. Matter Mater. Phys.* **2017**, *96*, 045402.

(44) Zimmer, G. Mos-technology,. *Microprocessing and Micro-programming* **1982**, *10* (2), 77−99.

(45) Park, J.; Kang, J.-H.; Liu, X.; Brongersma, M. L. Electrically tunable epsilon-near-zero (enz) metafilm absorbers,. *Sci. Rep.* **2015**, *5*, 15754.

(46) Brar, V. W.; Sherrott, M. C.; Jang, M. S.; Kim, S.; Kim, L.; Choi, M.; Sweatlock, L. A.; Atwater, H. A. Electronic modulation of infrared radiation in graphene plasmonic resonators,. *Nat. Commun.* **2015**, *6*, 7032.

(47) Nguyen, L. D.; Larson, L. E.; Mishra, U. K. Ultra-high speed modulation-doped field-effect transistors: a tutorial review,. *Proc. IEEE* **1992**, *80* (4), 494−518.

(48) Arafa, M.; Fay, P.; Ismail, K.; Chu, J. O.; Meyerson, B. S.; Adesida, I. High speed p-type sige modulation-doped field-effect transistors,. *IEEE Electron Device Lett.* **1996**, *17* (3), 124−126.

(49) Papadakis, G. T.; Atwater, H. A. Field-effect induced tunability in hyperbolic metamaterials,. *Phys. Rev. B: Condens. Matter Mater. Phys.* **2015**, *92*, 184101.

(50) Kim, Y. H.; Onishi, K.; Kang, C. S.; Cho, H.-J.; Choi, R.; Krishnan, S.; Akbar, M. S.; Lee, J. C. Thickness dependence of Weibull slopes of hfo lt;sub gt;2 lt;/sub gt; gate dielectrics,. *IEEE Electron Device Lett.* **2003**, *24* (1), 40−42.

(51) Caldwell, J. D.; Glembocki, O. J.; Francescato, Y.; Sharac, N.; Giannini, V.; Bezares, F. J.; Long, J. P.; Owrutsky, J. C.; Vurgaftman, I.; Tischler, J. G.; Wheeler, V. D.; Bassim, N. D.; Shirey, L. M.; Kasica, R.; Maier, S. A. Low-loss, extreme subdiffraction photon confinement via silicon carbide localized surface phonon polariton resonators,. *Nano Lett.* **2013**, *13* (8), 3690−3697.

(52) Iizuka, H.; Fan, S. Significant enhancement of near-field electromagnetic heat transfer in a multilayer structure through multiple surface-states coupling,. *Phys. Rev. Lett.* **2018**, *120*, 063901.

(53) Joulain, K.; Mulet, J.-P.; Marquier, F.; Carminati, R.; Greffet, J.-J. Surface electromagnetic waves thermally excited: Radiative heat transfer, coherence properties and casimir forces revisited in the near field,. *Surf. Sci. Rep.* **2005**, *57* (3), 59−112.

(54) Spitzer, W. G.; Kleinman, D.; Walsh, D. Infrared properties of hexagonal silicon carbide,. *Phys. Rev.* **1959**, *113*, 127−132.

(55) Boriskina, S. V.; Tong, J. K.; Huang, Y.; Zhou, J.; Chiloyan, V.; Chen, G. Enhancement and tunability of near-field radiative heat transfer mediated by surface plasmon polaritons in thin plasmonic films,. *Photonics* **2015**, *2* (2), 659−683.

(56) Wang, X. J.; Basu, S.; Zhang, Z. M. Parametric optimization of dielectric functions for maximizing nanoscale radiative transfer,. *J. Phys. D: Appl. Phys.* **2009**, *42* (24), 245403.

(57) Qin, H.; Zhao, B.; Nie, X.; Wen, J.; Yan, Y. Overview of sic power devices and its applications in power electronic converters,. *2013 IEEE 8th Conference on Industrial Electronics and Applications (ICIEA)* **2013**, 466−471.

(58) Pensl, G.; Morkoc, H.; Monemar, B.; Janzen, E. Silicon carbide, iii-nitrides, and related materials,. *Mater. Sci. Forum* **1998**, *264−268*, 3−89.

(59) Chelnokov, V.; Syrkin, A.; Dmitriev, V. Overview of sic power electronics,. *Diamond Relat. Mater.* **1997**, *6* (10), 1480−1484. Proceeding of the 1st European Conference on Silicon Carbide and Related Materials (ECSCRM 1996).

(60) Neudeck, P. G.; Spry, D. J.; Trunek, A. J. Measurements of breakdown field and forward current stability in 3c-sic pn junction diodes grown on step-free 4h-sic. In *Silicon Carbide and Related Materials 2005, Vol. 527 of Materials Science Forum*; Trans Tech Publications, 2006; pp 1335−1338.

(61) Fiorino, A.; Thompson, D.; Zhu, L.; Song, B.; Reddy, P.; Meyhofer, E. Giant enhancement in radiative heat transfer in sub-30 nm gaps of plane parallel surfaces,. *Nano Lett.* **2018**, *18* (6), 3711−3715.

(62) Yeh, P. *Optical Waves in Layered Media (Wiley Series in Pure and Applied Optics)*, 2nd ed.; Wiley-Interscience, 2005.

(63) Yeh, P. Electromagnetic propagation in birefringent layered media,. *J. Opt. Soc. Am.* **1979**, *69* (5), 742−756.

(64) Ben-Abdallah, P.; Joulain, K. Fundamental limits for noncontact transfers between two bodies,. *Phys. Rev. B: Condens. Matter Mater. Phys.* **2010**, *82*, 121419.

(65) Papadakis, G. T.; Fleischman, D.; Davoyan, A.; Yeh, P.; Atwater, H. A. Optical magnetism in planar metamaterial heterostructures,. *Nat. Commun.* **2018**, *9*, 296.

(66) Pérez-Rodríguez, J. E.; Pirruccio, G.; Esquivel-Sirvent, R. Spectral gaps in the near-field heat flux,. *Phys. Rev. Materials* **2019**, *3*, 015201.

(67) Zhao, B.; Zhang, Z. M. Enhanced photon tunneling by surface plasmonphonon polaritons in graphene/hbn heterostructures,. *J. Heat Transfer* **2017**, *139*, 022701.

(68) Kim, J.; Naik, G. V.; Emani, N. K.; Guler, U.; Boltasseva, A. Plasmonic resonances in nanostructured transparent conducting oxide films,. *IEEE J. Sel. Top. Quantum Electron.* **2013**, *19* (3), 4601907−4601907.

(69) Vasudev, A. P.; Kang, J.-H.; Park, J.; Liu, X.; Brongersma, M. L. Electro-optical modulation of a silicon waveguide with an "epsilon-near-zero" material,. *Opt. Express* **2013**, *21* (22), 26387−26397.

(70) Fu, C.; Zhang, Z. Nanoscale radiation heat transfer for silicon at different doping levels,. *Int. J. Heat Mass Transfer* **2006**, *49* (9), 1703−1718.

(71) Lee, H. W.; Papadakis, G.; Burgos, S. P.; Chander, K.; Kriesch, A.; Pala, R.; Peschel, U.; Atwater, H. A. Nanoscale conducting oxide plasmostor,. *Nano Lett.* **2014**, *14* (11), 6463−6468.

(72) Kafaie Shirmanesh, G.; Sokhoyan, R.; Pala, R. A.; Atwater, H. A. Dual-gated active metasurface at 1550 nm with wide (300) phase tunability,. *Nano Lett.* **2018**, *18* (5), 2957−2963.

(73) West, P., Ishii, S., Naik, G., Emani, N. K., Shalaev, V. M., Boltasseva, A., Searching for better plasmonic materials. *Laser Photonics Rev.* **2010**, *4*, 795−808.

(74) Naik, G. V.; Kim, J.; Boltasseva, A. Oxides and nitrides as alternative plasmonic materials in the optical range,. *Opt. Mater. Express* **2011**, *1* (6), 1090−1099.

(75) Boltasseva, A.; Atwater, H. A. Low-loss plasmonic metamaterials,. *Science* **2011**, *331* (6015), 290−291.

(76) Krasavin, A. V.; Zayats, A. V. Photonic signal processing on electronic scales: Electro-optical field-effect nanoplasmonic modulator,. *Phys. Rev. Lett.* **2012**, *109*, 053901.

(77) Nicollian, E.; Brews, J. R. *MOS (Metal Oxide Semiconductor) Physics and Technology*,15th ed.; Wiley: New York, NY, 1982.

(78) Choyke, W. J.; Patrick, L. Luminescence of donor-acceptor pairs in cubic sic,. *Phys. Rev. B* **1970**, *2*, 4959−4965.

(79) Chiloyan, V.; Garg, J.; Esfarjani, K.; Chen, G. Transition from near-field thermal radiation to phonon heat conduction at sub-nanometre gaps,. *Nat. Commun.* **2015**, *6*, 6755.

(80) Kim, K.; Song, B.; Fernndez-Hurtado, V.; Lee, W.; Jeong, W.; Cui, L.; Thompson, D.; Feist, J.; Reid, M. T. H.; Garca-Vidal, F. J.; Cuevas, J. C.; Meyhofer, E.; Reddy, P. Radiative heat transfer in the extreme near field. *Nature* **2015**, *528*, 387.

(81) Papadakis, G. T.; Narang, P.; Sundararaman, R.; Rivera, N.; Buljan, H.; Engheta, N.; Soljačić, M. Ultralight angstrom-scale optimal optical reflectors,. *ACS Photonics* **2018**, *5* (2), 384−389.

(82) Falkovsky, L. A. Optical properties of graphene,. *Journal of Physics: Conference Series* **2008**, *129* (1), 012004.

(83) Fiorino, A.; et al. Nanogap near-field thermophotovoltaics,. *Nat. Nanotechnol.* **2018**, *13* (9), 806.

(84) Chen, K.; Zhao, B.; Fan, S. Mesh: A free electromagnetic solver for far-field and near-field radiative heat transfer for layered periodic structures,. *Comput. Phys. Commun.* **2018**, *231*, 163−172.